Experimental Analysis on Ultrasonic Resistance Spot Welding of Aluminum Alloys

Ultrasonic vibration during resistance spot welding improved the mechanical properties and microstructure of dissimilar and similar aluminum alloy welds

BY H. KWON, U. SHAH, X. LIU, J. MALPICA, P. LESTER, AND H. BONAM

Abstract

A recently developed hybrid joining process known as ultrasonic resistance spot welding (URW) was used on various pairs of similar and dissimilar aluminum (Al) alloys with different thicknesses, including AA5182–AA5182, AA6111–AA6111, AA7075–AA6111, and AA7075–AA5182, and comprehensively studied. Compared to conventional resistance spot welding (RSW), URW of the alloys showed consistently enhanced mechanical behavior in lap shear and cross-tension tests. This can be attributed to the multiple perspectives on microstructure improvements. For different stacks of Al alloys and welding conditions, nugget formation was promoted with a larger nugget size in URW. In the nugget center, ultrasonically assisted (UA) vibration facilitated the formation of an equiaxed crystal zone. At the nugget boundary, URW showed a narrower coarse columnar zone and partially melted zone, which are associated with the lowest hardness in the weld. Specifically in dissimilar Al welds, UA vibration moved the nugget more centered toward the weld interface. These microstructure improvements indicated UA vibration can homogenize temperature and elemental distribution, which modifies solidification behavior.

Keywords

- Power Ultrasound
- Resistance Spot Welding
- Aluminum
- Microstructure
- Hardness

https://doi.org/10.29391/2023.102.017

Introduction

Statistics have shown that the transportation industry is the major contributor to greenhouse gas emissions (Ref. 1). Structure weight reduction is one of the most effective approaches to reducing greenhouse gas emissions (Refs. 2, 3). Lightweighting can be achieved by utilizing aluminum (Al) alloys due to their low density and higher strength-to-weight ratio (Ref. 4). On the other hand, the joining of Al alloys is challenging due to their inherent oxide layers and susceptibility to solidification defects, such as cracking and porosity (Ref. 5).

Ultrasonic spot welding (USW) is a solid-state welding process that is widely used for joining various kinds of thin Al alloy sheets and foils (Refs. 6, 7). The lateral motion of the sonotrode introduces shearing and plastic deformation at the interface between sheets, which leads to the breakage of surface oxides and the creation of metallic bonding (Ref. 8). Compared with resistance spot welding (RSW), USW can greatly improve welding energy efficiency (Ref. 9). However, high energy is required to weld materials with high hardness and large thickness, which can be challenging due to the power limitation of generally available ultrasonic transducers (Ref. 7).

RSW of Al is more difficult than of steel as Al has three times higher electrical and thermal conductivity (Ref. 10). The inherent Al oxide layer creates inconsistencies and faster electrode degradation (Ref. 11). Many efforts have been introduced to improve Al weld quality. Crinon et al. (Ref. 12) reported that relative rotation of 0.2 deg can significantly drop the sheet-to-sheet electrical contact resistance. Chang et al. (Ref. 13) showed that the application of an additional high forging force immediately after the passage of the current can improve the fatigue life of AA5182 RSW welds. Naimi et al. (Ref. 14) increased the shear tensile strength of the AA1050 weld through surface modification with NaOH picking. Luo et al. (Ref. 15) applied preheating during the RSW of AA5052 and showed higher strength. In addition, electrode design studies have focused on the fracture of surface oxide layers. Deng et al. (Ref. 16) studied the multiring domed electrode with

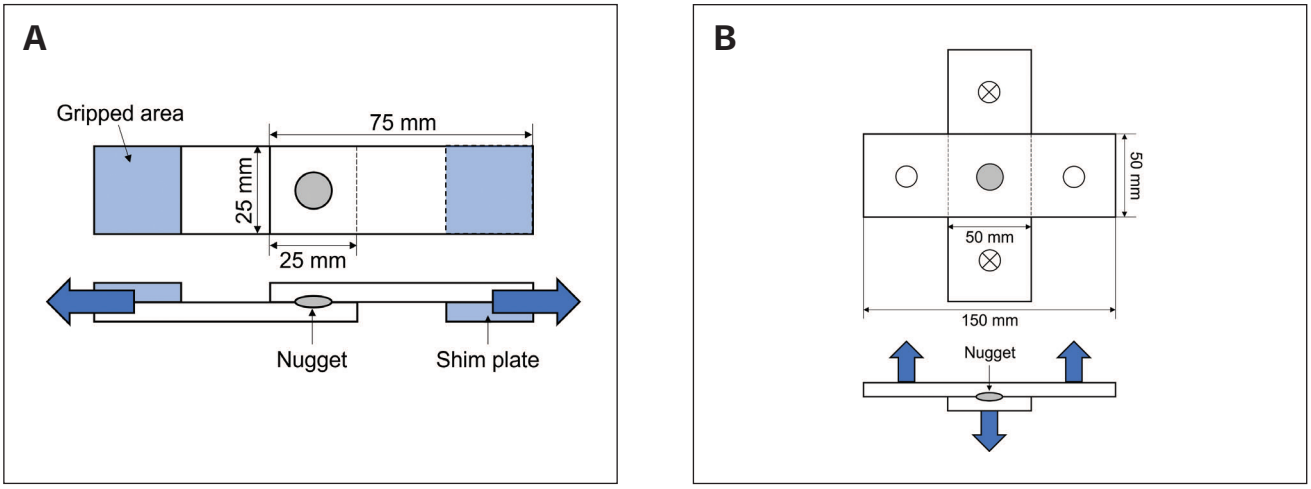

Fig. 1 — Dimensions of lap shear tensile specimen (A) and cross-tension specimen (B).

Table 1 — Chemical Composition of Al Alloy Sheets

Wt-%	Si	Fe	Cu	Mn	Mg	Cr	Zn	Ti
AA7075-T6 (Ref. 23)	≦ 0.4	≦ 0.5	1.2–2.0	N/A	2.1–2.9	0.18–0.28	5.1–6.1	≦ 0.3
AA6111-T4 (Ref. 24)	0.6–0.9	≦ 0.4	0.6–0.9	0.05–0.25	0.7–1.0	0.05–0.2	≦ 0.25	≦ 0.1
AA5182-O (Ref. 25)	≦ 0.2	≦ 0.35	≦ 0.15	0.2–0.5	4.0–5.0	≦ 0.1	≦ 0.25	≦ 0.1

concentric ring protrusions on top, which reduced distortion and coarse columnar zone (CCZ) size in the nugget. Wang et al. (Ref. 17) developed the Newton ring (NTR) electrode and observed greatly improved mechanical properties of AA5182 without severe expulsion. Li et al. (Ref. 18) modified the surface morphology of the NTR electrode with two concentric rings on top of the original ring. Consistent nuggets were obtained for up to 210 welds. Another RSW improvement approach was to modulate liquid flow in the nugget. Magnetically assisted RSW of 5xxx alloys (Ref. 19), 6xxx alloys (Ref. 20), and 7xxx alloys (Ref. 21) have been studied. Permanent magnets were applied on both the top and bottom electrodes and induced circumferential magnetic force. Combined with the intrinsic electromagnetic force generated by the RSW current, the flow in a liquid nugget can be modified to refine the grain structures and remove defects.

Shah and Liu (Ref. 5) recently developed a hybrid joining method known as ultrasonic-assisted resistance welding (URW) to combine the advantages of USW and RSW. During the process, ultrasonic vibration was applied perpendicular to the sheet-to-sheet contact interface simultaneously when an electrical current was passing through. The URW welds have shown improved mechanical properties for AA6061-T6 alloys, including a larger nugget and refined microstructure. In this study, the effectiveness of URW on several similar and dissimilar Al alloys was investigated. The effects of ultrasonic energy, dissimilar Al composition, and sheet thickness on nugget microstructure and weld mechanical properties were evaluated.

Experimental Details

Al alloy stacks including AA7075 (2.8 mm [0.11 in.]), AA6111 (2.0 mm [0.08 in.]), and AA5182 (1.1 mm [0.04 in.] and 1.5 mm [0.06 in.]), were investigated. The chemical compositions of the three materials are listed in Table 1. Mechanical and physical properties are provided in Table 2. The URW system was developed based upon a 60 Hz alternating current 100 kVA press-type RSW machine with single-phase control. The electrode was made of a RWMA Class 1 material with a

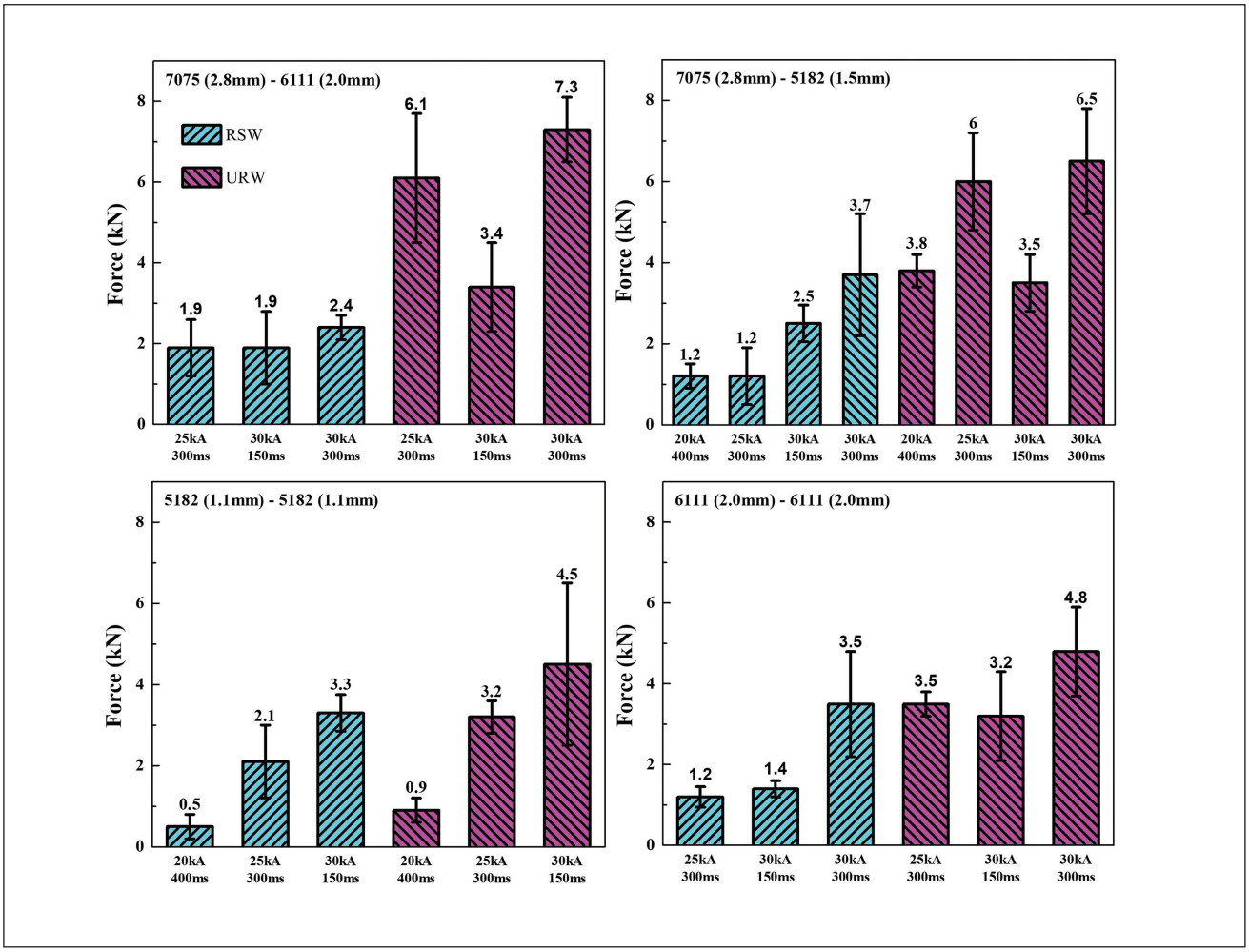

Fig. 2 — Comparison of maximum force during lap shear tensile tests between RSW and URW welds of dissimilar and similar Al alloys at various conditions.

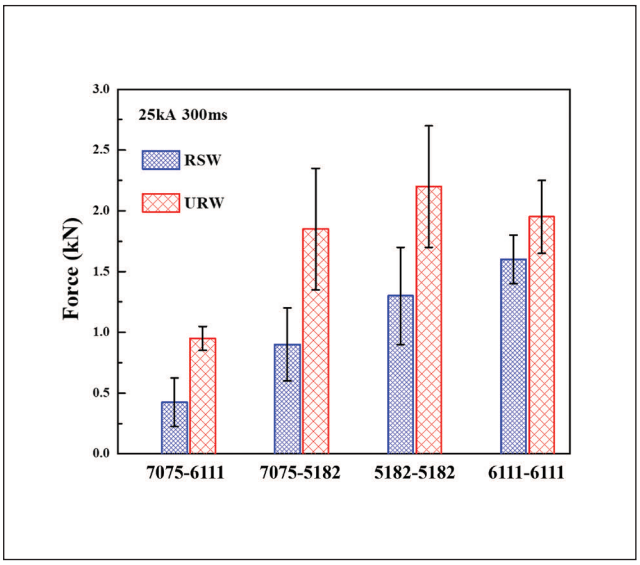

Fig. 3 — Comparison of maximum force during cross-tension tests of dissimilar and similar Al RSW and URW welds.

flat cylindrical shape and a 12 mm (0.47 in.) tip diameter. A piezoelectric ultrasonic transducer was directly connected to the bottom electrode, which accordingly served as the sonotrode to introduce perpendicular ultrasonic vibration to the workpiece contact interface. The ultrasound frequency was 19.4 kHz, and the peak-to-peak vibration amplitude was 34 μm in the unloaded condition. The ultrasonic power was maintained at 700 W during the welding process. Vibration started with the welding current and continued until the current stopped. Ultrasonic energy varied between 105 and 280 J, depending on the welding time. More details about the system are provided in Refs. 5 and 22.

During the process, the squeeze and hold time were kept at 300 and 200 ms, respectively. Welding current and time varied at different levels, as provided in Table 3. Welding force was maintained at 5.2 kN.

For the welded samples, lap shear tensile tests were carried out at a rate of 2 mm/min along the sample transverse direction. Restraining shims were placed to ensure coplanar loading. Cross-tension tests were performed according to AWS D8.9, *Test Methods for Evaluating the Resistance Spot Welding Behavior of Automotive Sheet Steel Materials* at a

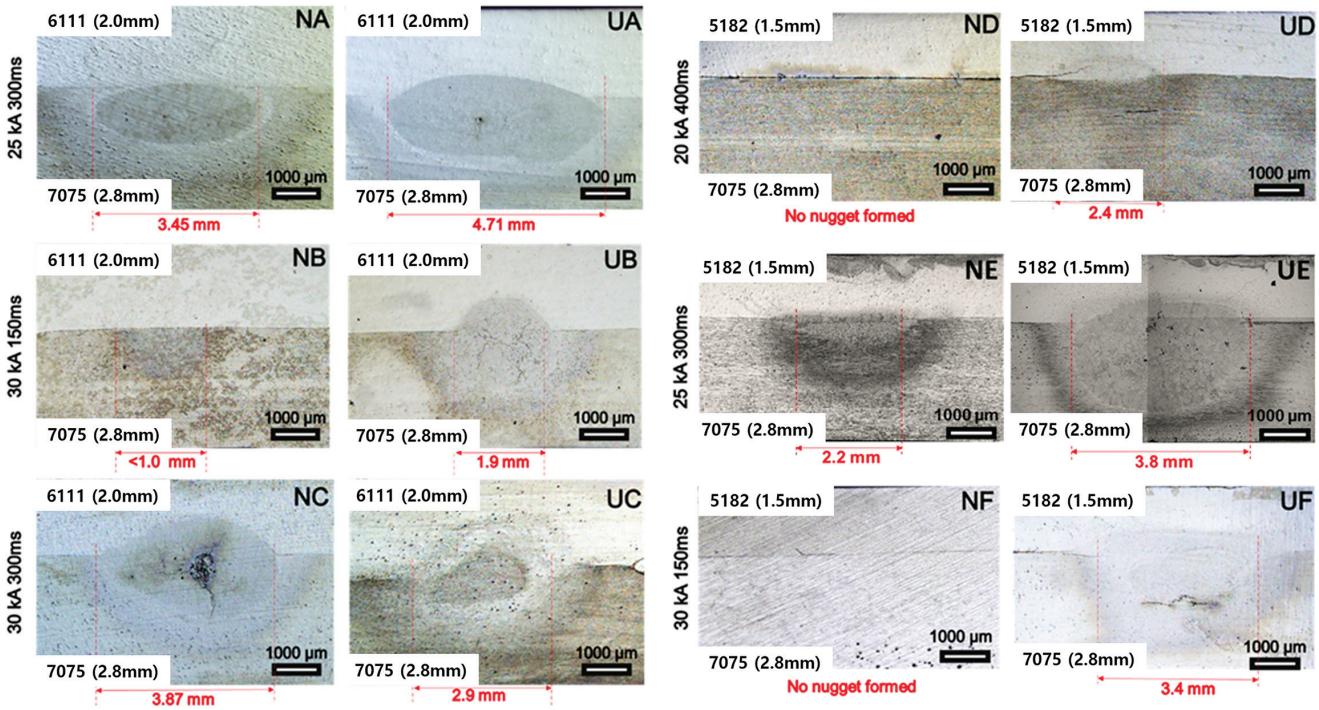

Fig. 4 — RSW and URW weld nugget profiles of dissimilar Al alloys obtained at various welding conditions. Sample designation corresponds to each welding condition described in Table 1, where RSW welds are denoted as NX and URW welds are denoted as UX.

Table 2 — Mechanical and Physical Properties of Al Alloy Sheets

	Yield Strength (Rp 0.2)	Ultimate Tensile Strength	Elastic Modulus	Thermal Conductivity	Coefficient of Thermal Expansion	Electrical Resistivity
AA7075-T6 (Ref. 23)	≧ 480 MPa	≧ 540 MPa	70 GPa	130 W/mK	$23.4*10^{-6}$ K^{-1}	$5.15*10^{-8}$ o-m
AA6111-T4 (Ref. 24)	≧ 160 MPa	≧ 300 MPa	70 GPa	160–190 W/mK	$23.4*10^{-6}$ K^{-1}	$3.3–3.8*10^{-8}$ o-m
AA5182-O (Ref. 25)	≧ 130 MPa	≧ 270 MPa	69.6 GPa	126 W/mK	$23.4*10^{-6}$ K^{-1}	$5.6*10^{-8}$ o-m

speed of 5 mm (0.20 in.)/min. The sample dimensions are provided in Fig. 1. Mechanical tests were performed at least three times for each sample. Metallographic samples were sectioned along the weld center and grounded, polished, and etched following standard preparation procedures for optical microstructural analysis. The cross-sectional nugget size and width of each microstructural zone were measured via ImageJ software. Vickers microhardness analysis was performed at 25 g (0.05 lb) of load with 100 µm indent spacing.

Results

Mechanical Behavior

Figure 2 compares the maximum load of the similar and dissimilar Al welds during lap shear tensile tests. The majority of the URW welds showed higher strength than the RSW welds. Between AA7075 (2.8 mm) and AA6111 (2 mm) at 30 kA for 300 ms, URW strength was around three times that of

Table 3 — Weld Parameters for Different Pairs of Al Alloys

	Designation	Ultrasonic	Weld Current (kA)	Weld Time (ms)
		Dissimilar Stacks		
AA7075 (2.8 mm)-AA6111 (2.0 mm)	NA	Off	25	300
	NB	Off	30	150
	NC	Off	30	300
	UA	On	25	300
	UB	On	30	150
	UC	On	30	300
AA7075 (2.8 mm)-AA5182 (1.5 mm)	ND	Off	20	400
	NE	Off	25	300
	NF	Off	30	150
	NG	Off	30	300
	UD	On	20	400
	UE	On	25	300
	UF	On	30	150
	UG	On	30	300

RSW. When increasing the electrical current from 25 to 30 kA while reducing the welding time from 400 to 150 ms, the ultrasonic enhancement was less effective. Between AA7075 (2.8 mm) and AA5182 (1.5 mm), up to a 400% increase in the mechanical strength was achieved at 25 kA for 300 ms in the URW weld. However, if the current was below 20 kA, the benefit was less obvious. In AA5182 (1.1 mm) and AA6111 (2 mm), the lap shear tensile strength improvements of URW were smaller than with dissimilar Al pairs.

Figure 3 compares the cross-tension testing results when all of the welds were performed at 25 kA for 300 ms. In RSW, similar stacks showed higher cross-tension strength than dissimilar stacks. Among the similar stacks, the cross-tension strength of AA5182 was lower than that of AA6111. A considerable amount of strength improvement in the AA5182 weld was achieved in URW, where the average was around 43% higher than with RSW. Comparing similar and dissimilar Al welds, the ultrasonic improvement on cross-tension strength was more significant in dissimilar stacks.

Weld Microstructure

None of the as-welded samples showed signs of expulsion and cracks on the surfaces. Figure 4 compares the overview optical micrographs of dissimilar Al RSW and URW weld cross sections obtained at various welding conditions. Between AA6111 and AA7075 at 30 kA for 150 ms, RSW showed only a point bonded interface, whereas URW achieved a small nugget. At 30 kA for 300 ms, RSW seemed to show a larger nugget size but contained a large weld defect at the interface. At 25 kA for 300 ms, both RSW and URW formed a nugget without macroscopic weld discontinuities. However, the RSW nugget was almost completely on the AA7075 side, whereas the URW nugget was more evenly distributed across the interface. Similar trends were observed in AA5182 to AA7075 welds, as shown in the right columns of the images in Fig. 4. URW showed larger, fully bonded, and more evenly distributed nuggets between the sheets.

Table 3 — continued

	Designation	Ultrasonic	Weld Current (kA)	Weld Time (ms)
		Similar Stacks		
AA5182-AA5182 (1.1 mm)	NH	Off	20	400
	NI	Off	25	300
	NJ	Off	30	150
	UH	On	20	400
	UI	On	25	300
	UJ	On	30	150
AA6111-AA6111 (2.0 mm)	NK	Off	25	300
	NL	Off	30	150
	NM	Off	30	300
	UK	On	25	300
	UL	On	30	150
	UM	On	30	300

AA6111–AA7075 weld microstructures are compared in more detail in Fig. 5. In RSW, the nugget was almost completely formed on the AA7075 side. At the nugget center, the equiaxed crystal zone (ECZ) was observed with a bimodal structure consisting of equiaxed dendrites and nondendritic eutectic phases. The center ECZ was surrounded by a fine dendritic zone (FDZ) and had a CCZ at the periphery of the nugget. The CCZ and partially melted zone (PMZ) were wider on the AA7075 side. The heat-affected zone (HAZ), showing a darker color due to overaging of precipitates, was also wider on the AA7075 side.

In the URW weld, the nugget position was slightly balanced toward the AA6111 side, as in Fig. 5G. Compared with the ECZ in the RSW nugget, the higher portion of equiaxed α-Al dendrites was observed in URW, as in Fig. 5H. In the meantime, the amount of nondendritic regions decreased. A similar phenomenon has been reported with the magnetically assisted RSW process and was explained based on liquid circulation by magnetic force (Ref. 19). In the URW nugget, the ECZ's size was larger. At the nugget boundary, the CCZ's thickness was reduced. Figure 6 shows the PMZ's thickness was smaller in both the AA7075 and AA6111 sides in URW than in the RSW condition. Similar observations on the PMZ's thickness reduction under ultrasonically assisted (UA) vibration were also noticed in the AA6061 welds (Ref. 5).

Figure 7 shows detailed optical macrographs of the AA7075–AA5182 weld cross section at the condition of 25 kA for 300 ms. A small and shallow melted nugget was observed in RSW, as in Fig. 7A. The nugget center was shifted toward the AA7075 side with deeper penetration. This uneven distribution of nugget can directly decrease cross-tension strength. Literature shows that in RSW welds of dissimilar thickness, the final solidification line was located in the geometrical center of the stack, rather than at the sheet-to-sheet interface, if electrode size was the same on both sides (Ref. 26). The electrical resistivity of AA7075 was similar to that of AA5182, as shown in Table 2. Accordingly, the thicker AA7075 sheet had higher bulk resistance than AA5182's, which led to deeper penetration into the AA7075 side. The lower solidus temperature of AA7075 corresponded to a faster melting rate, which further shifted the nugget. In Fig. 7B–E, a black zigzag line can be clearly noticed at the interface, indicating a not fully bonded condition. Above the zigzag line, a CCZ was observed. Below the zigzag line, the equiaxed solidification structure existed in the shifted nugget on the AA7075 side.

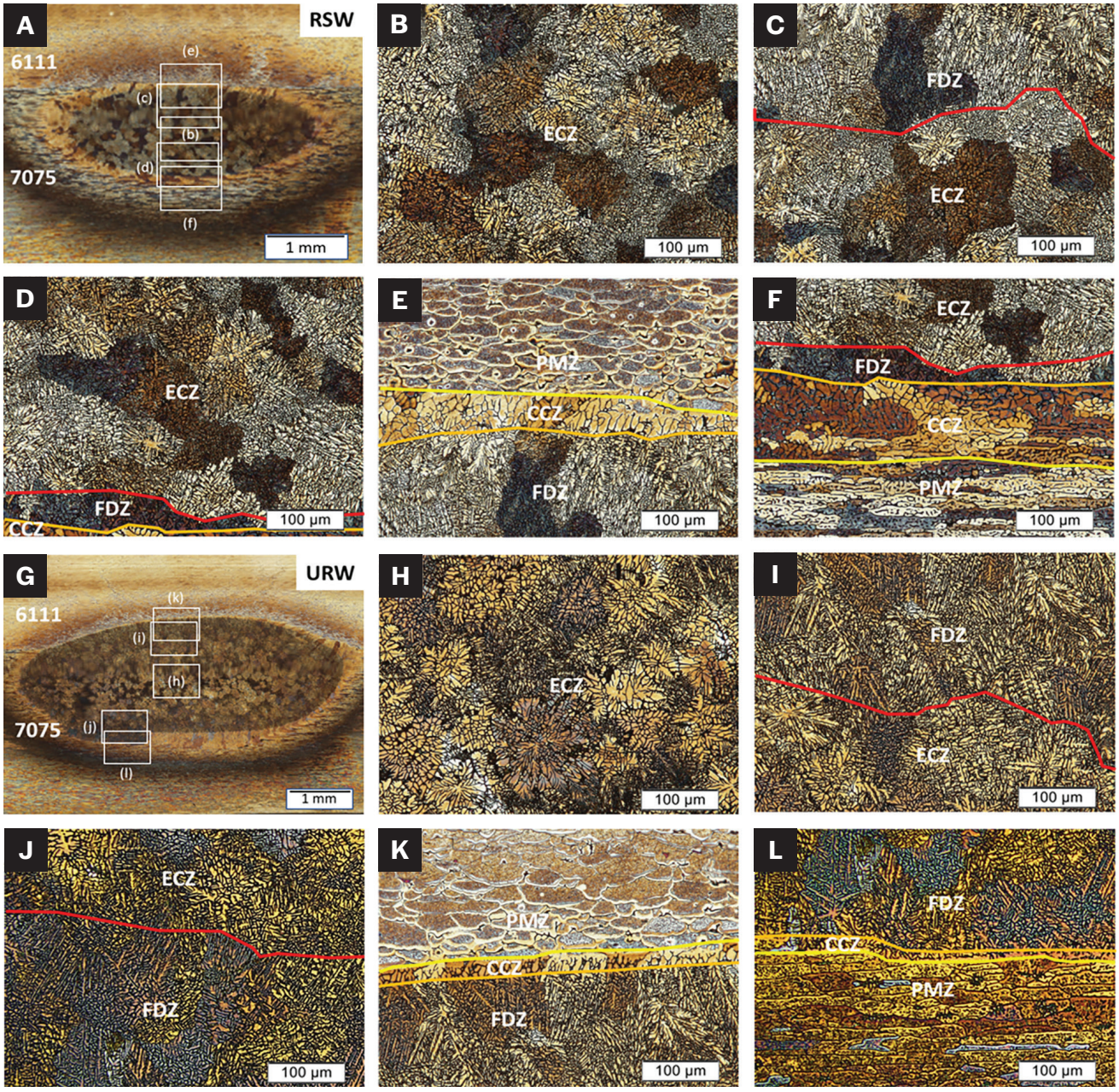

Fig. 5 — Optical micrographs of AA6111–AA7075 dissimilar nugget cross section in RSW (A–F) and URW (G–L). Both samples obtained at the same welding condition of 25 kA for 300 ms.

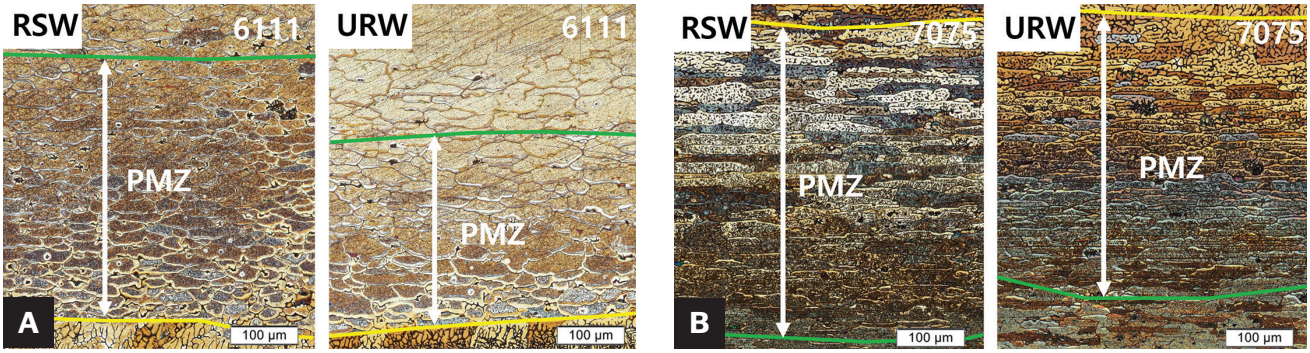

Fig. 6 — Comparison of PMZ in RSW and URW welds of AA6111–AA7075: A — AA6111 side; B — AA7075 side.

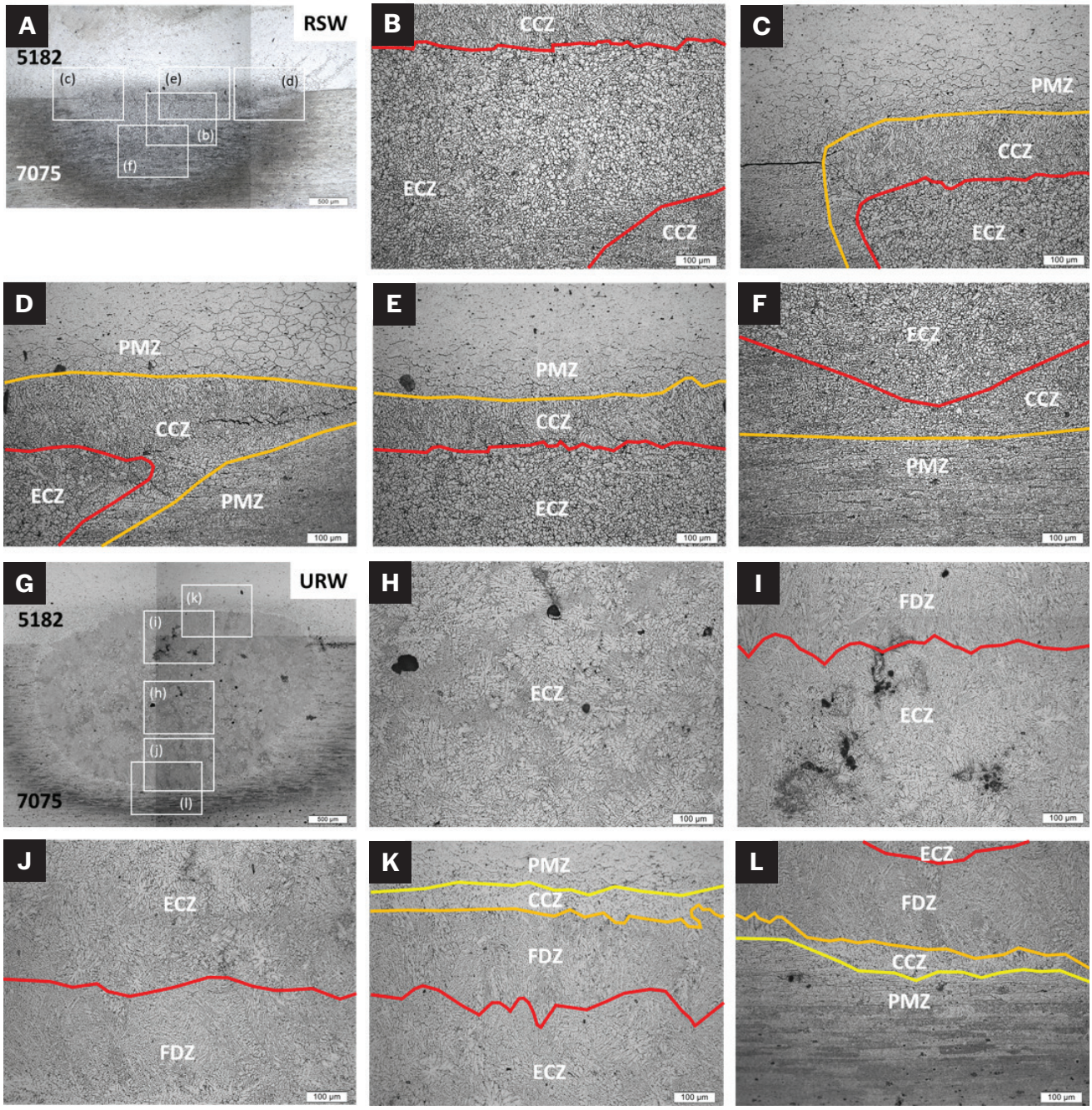

Fig. 7 — Optical micrographs of AA5182–AA7075 dissimilar nugget cross section in the RSW (A–F) and URW weld (G–L). Both samples obtained at the same welding condition of 25 kA for 300 ms.

Outside of the nugget, both the PMZ and HAZ were wider on the AA7075 side than on the AA5182 side.

In contrast, URW achieved a sound elliptical-shaped nugget, as in Fig. 7G–I. The nugget size was larger than in conventional RSW, and the center of the nugget was better balanced at the sheet-to-sheet interface, which was consistent with the AA7075–AA6111 weld. The URW nugget contained an ECZ in the center, surrounded by an FDZ on both AA5182 and AA7075 sides. The ECZ in URW welds contained a bimodal structure, with equiaxed α-Al dendrites and non-dendritic secondary phases distributed in between. Similar to AA7075–AA6111 welds, the thickness of the CCZ at the nugget boundary was narrower in URW. Figure 8 shows the PMZ was narrower in URW at both the AA5182 and AA7075 sides, which is consistent with AA6111–AA7075 welds.

Figure 9 compares the RSW and URW welds of AA5182. The nugget size increased considerably in URW conditions. Both nuggets contained a two-layer structure. However, the specific microstructure was different. In RSW, the FDZ in the center was surrounded by the CCZ. In contrast, the URW nugget structure was neither columnar nor equiaxed dendrites, as in Fig. 9E and F. Particularly in the center, the

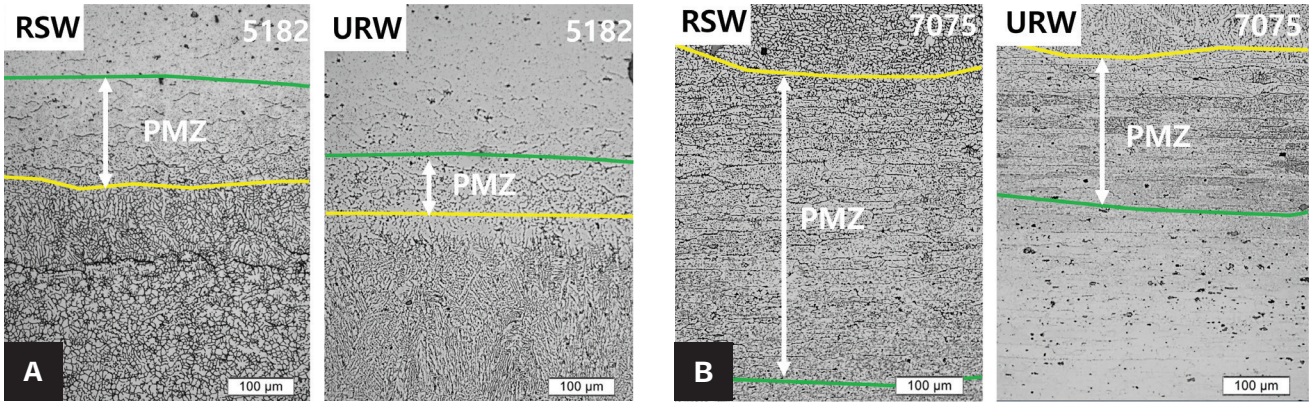

Fig. 8 — Comparison of PMZ in RSW and URW welds of AA5182–AA7075: A — AA5182 side; B — AA7075 side.

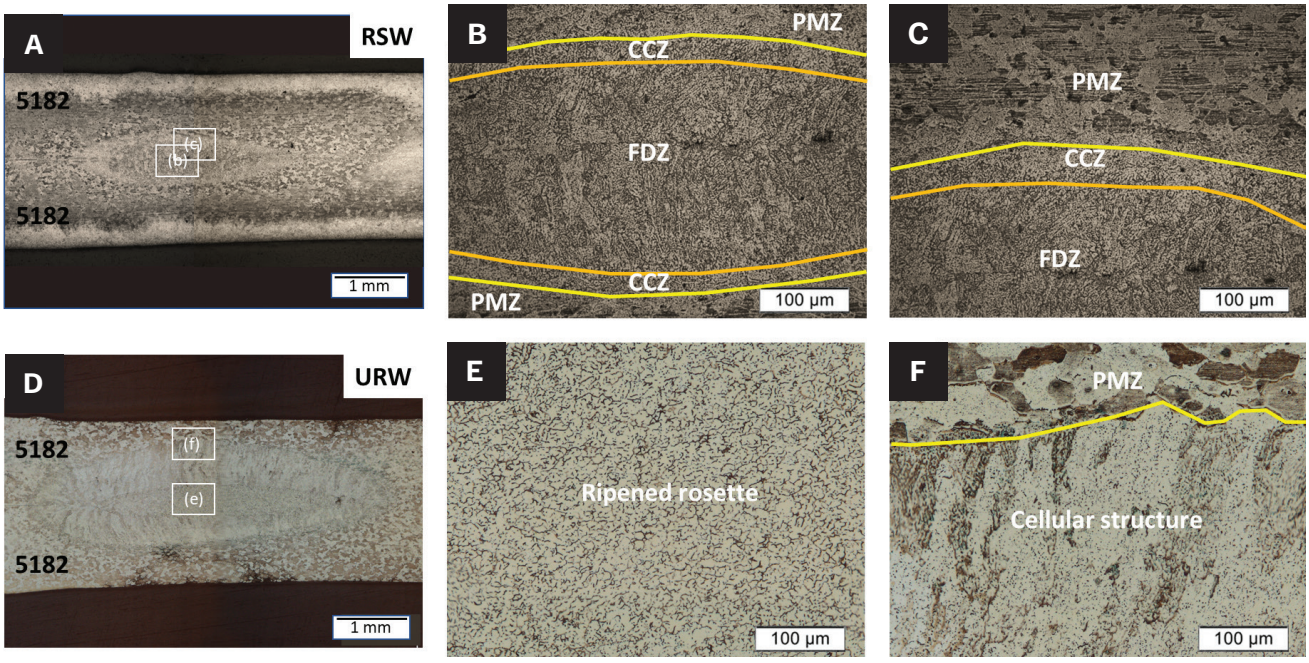

Fig. 9 — Optical micrographs of AA5182 nugget cross section after RSW (A–C) and URW (D–F). Both samples obtained at the same welding condition of 25 kA for 300 ms.

structure presented a ripened rosette or spheroid morphology in between the cellular structure. A similar structure has been described by Flemings (Ref. 28) when shear deformation is applied during the solidification of semisolid slurries. This is referred to as nondendritic solidification and is commonly observed in semisolid metal forming processes. In URW, the UA vibration also applied a shear action on the dendrites in the partially solidified nugget, showing the unique nondendritic structure when fully solidified. The PMZ in AA5182 welds, as shown in Fig. 10, were overall narrow due to their small solidification ranges. Consistent with dissimilar Al stacks, the PMZ in the URW weld was narrower than in the RSW weld.

RSW and URW weld cross sections of AA6111 are shown in Fig. 11. RSW contained only columnar dendrites in the nugget center. In comparison, an ECZ with a bimodal structure was achieved in the URW nugget center. Further outside, the CCZ's thickness was also noticed to be smaller, which is consistent with the dissimilar Al weld results.

Hardness Distribution

Figures 12A and B show the hardness maps of RSW and URW AA7075–AA6111 stacks with the corresponding optical micrographs. The map clearly shows the nugget location surrounded by dissimilar base metals with different hardnesses. The volumetric dilution of AA6111 in AA7075 was distinguishable in URW. Base material AA7075-T6 contained a significantly higher hardness than that of AA6111-T4, and hardness in the nugget was in between the two materials. Combining the hardness maps with the microstructure distribution in the nugget, hardness was the highest in the ECZ followed by the FDZ and then the CCZ. Note that the CCZ

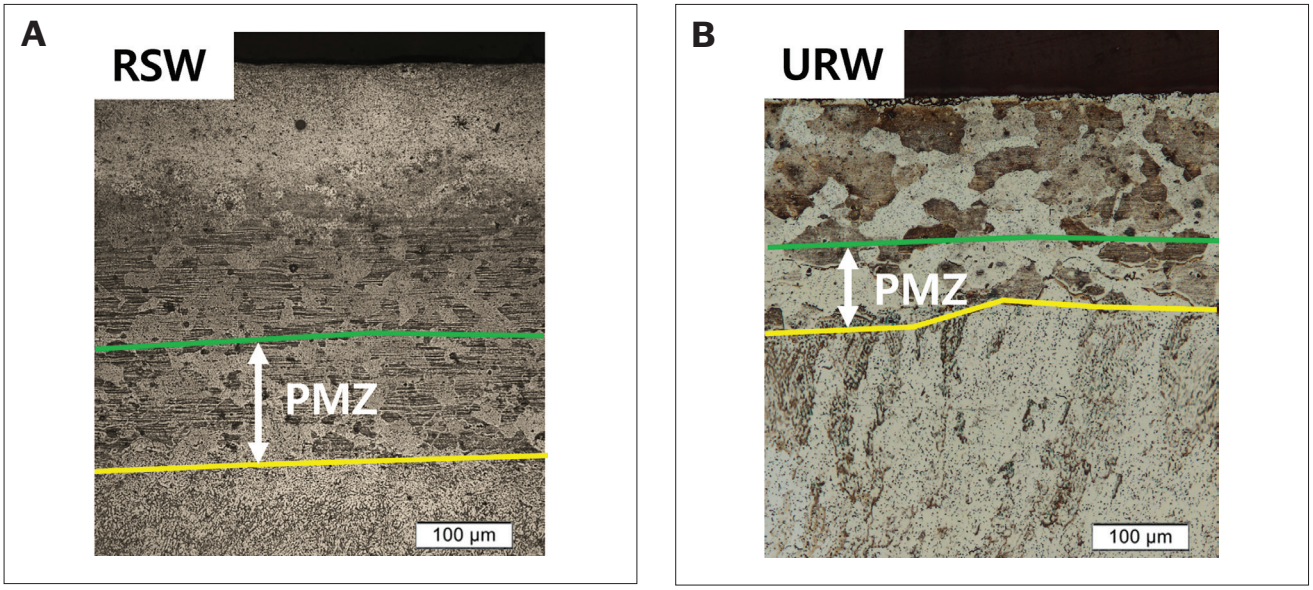

Fig. 10 — Comparison of PMZ in AA5182 welds: A — RSW; B — URW.

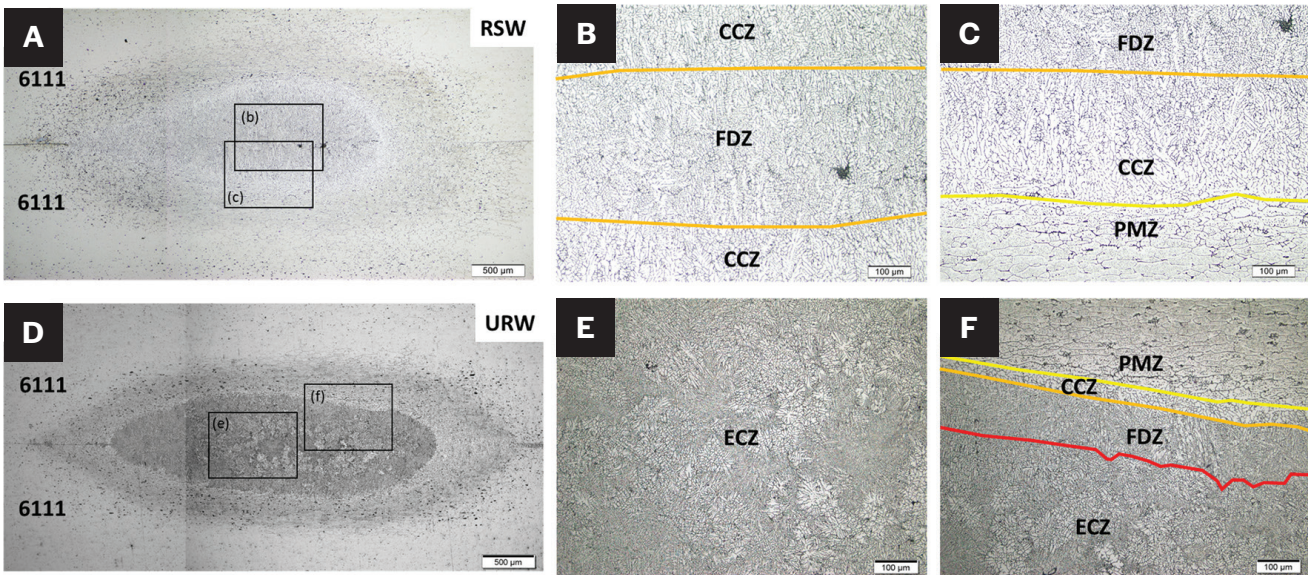

Fig. 11 — Optical micrographs of AA6111 nugget cross section in RSW (A–C) and URW (D–F). Both samples were obtained at the welding condition of 25 kA for 300 ms.

at the nugget boundary showed lower hardness than the nugget and the HAZ on both the AA7075 and AA6111 sides. This is because the CCZ is a coarse structure with less alloy content (Ref. 29). The low local hardness would make the CCZ most prone to failure under stress.

Comparing URW with RSW, the hardness along the nugget periphery was relatively higher in URW conditions. This is consistent with the microstructures in Fig. 5E, F, K, and L: The thickness of the CCZ was greatly reduced under UA vibration. The overall hardness of the fusion zone (FZ) in RSW was higher than that of URW. Figure 12C plots the hardness variation along the vertical line through the nugget center from the AA7075 to the AA6111 side and provides a more quantitative comparison.

The AA5182 hardness maps and corresponding macrographs are provided in Fig. 13. Quantitative hardness values along the weld centerline from the bottom to the top surface in the URW and RSW welds were compared in Fig. 13C. The overall hardness ranged from 73 to 79 HV in the FZ, which is similar to that of O-tempered base metal sheets. Mapping with microstructure distribution in the RSW nugget, the hardness was slightly higher in the FDZ than in the CCZ. The maximum hardness was located at the outer-layer structure in URW. In the URW center, which was characterized by the nondendritic rosette structure, the hardness was slightly lower than the FDZ in the RSW weld center. However, the difference was less than 5 HV.

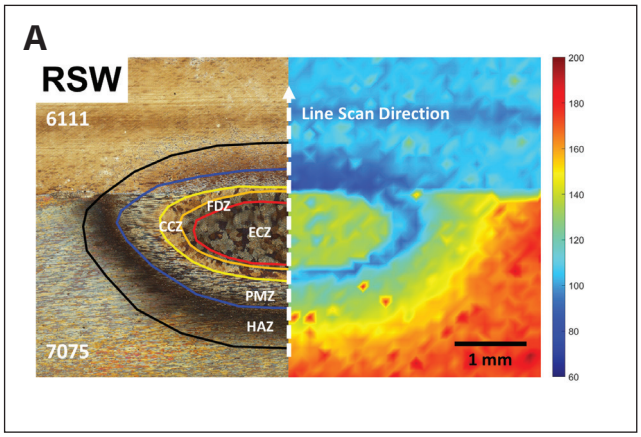

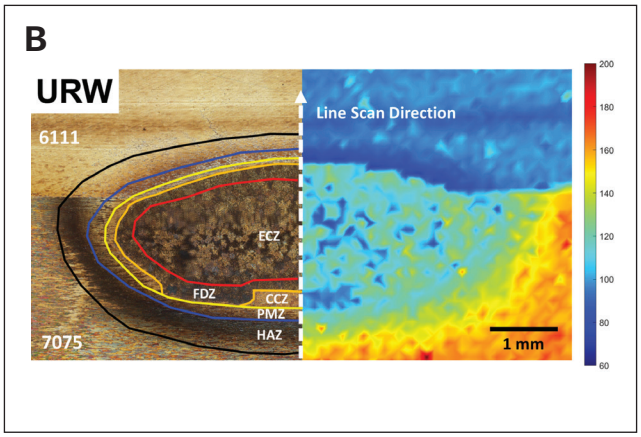

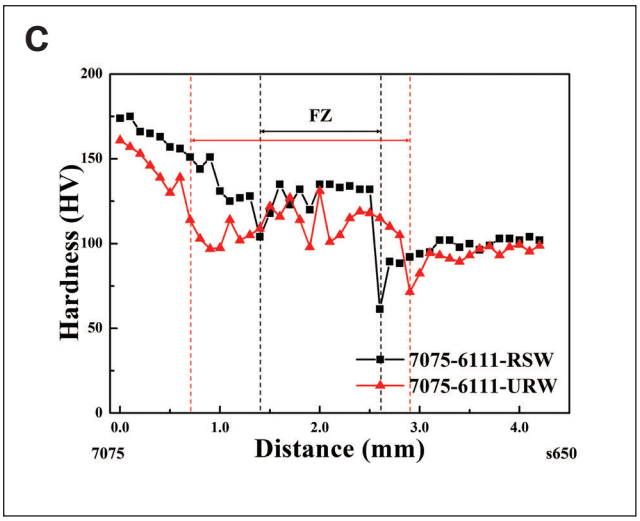

Fig. 12 — Hardness distribution of AA7075–AA6111 welds in RSW (A) and URW (B) as well as hardness variation (C) along the white dashed arrow from AA7075 to AA6111 side in A and B.

Fracture Surface Analysis

In RSW, eight fracture modes exist, according to AWS D8.2M, *Specification for Automotive Weld Quality—Resistance Spot Welding of Aluminum* (Ref. 30). The button pullout and interfacial fracture, which were respectively driven by shear stress at the sheet-to-sheet interface and tensile stress at the nugget circumference (Ref. 31), were commonly observed. Figure 14 shows the fracture surfaces after lap shear tensile tests for different pairs of Al alloys. The fracture surface generally contained two rings: inside and outside. The inside ring was the actual fully bonded region while only partial bonding occurred at the outside ring. The fracture surfaces were similar in AA7075–AA6111 and AA7075–AA5182 welds. Both exhibited interfacial failure in URW and RSW welds. Only the fracture surfaces on the AA7075 side of AA7075–AA6111 welds are present in Figs. 14A and B.

Discussion

Ultrasonic Effects on Weld Microstructure and Hardness

The biased nugget position of the AA6111–AA7075 RSW weld in Fig. 5A was due to lower electrical resistivity and the smaller thickness of AA6111. Accordingly, higher resistance heating was generated on the AA7075 side. The nugget position partially explains the lowest cross-tension strength of the AA6111–AA7075 RSW weld among all the pairs. It was also consistent with the hardness map in Fig. 12A that the faying interface mainly consisted of the CCZ and had the lowest hardness. The higher resistance heating promoted the growth of the CCZ on the AA7075 side. It also contributed to the wider HAZ on the AA7075 side from a slower cooling rate and longer time for precipitate growth. Similar results were noted in the RSW of AA7075–AA6061 (Ref. 32), where the major alloying elements of AA6061 were similar to those of AA6111. The PMZ was formed at the solidification temperature range, and partial melting occurred at the eutectic phases and grain boundaries, where the low-melting elements segregated. The wider PMZ of the AA7075 side in Fig. 6 was due to its larger solidification range and the presence of low-melting eutectic phases.

In comparison to URW, UA vibration can produce a more symmetric weld nugget and penetrate deeper into the lower-resistance AA6111 side, as shown in Fig. 5G. In the previous study (Ref. 5), the peak temperature in URW was lower than in RSW. Furthermore, the total dynamic resistance in URW was lower than in RSW (Ref. 3). These findings indicate that the additional ultrasonic energy input can be a minor factor in overall heating. Based on solidification theories, cellular or columnar dendritic growth dominated under a high thermal gradient at the solid-liquid interface (Ref. 34). The equiaxed solidification structure was promoted under a small temperature gradient (Ref. 35). Considering acoustic cavitation and streaming effects, the temperature distribution in the nugget center was homogenized from the enhanced convection of molten metal (Ref. 27). The mixture of high-temperature metal in the center and newly melted low-temperature metal near the nugget boundary were promoted, which reduced the temperature gradient.

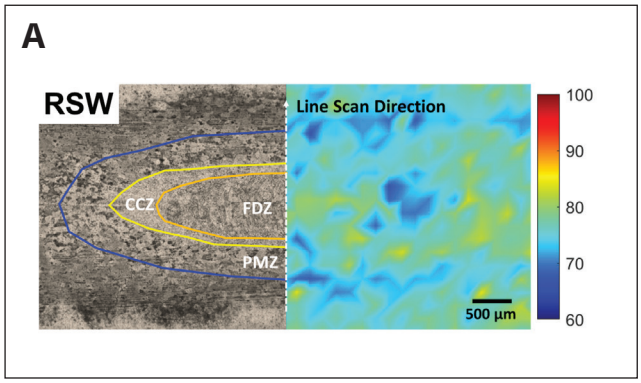

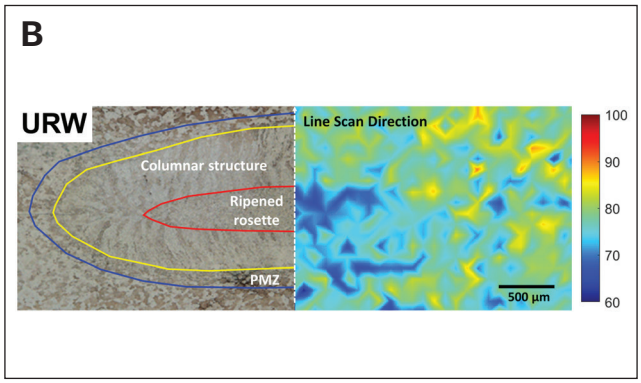

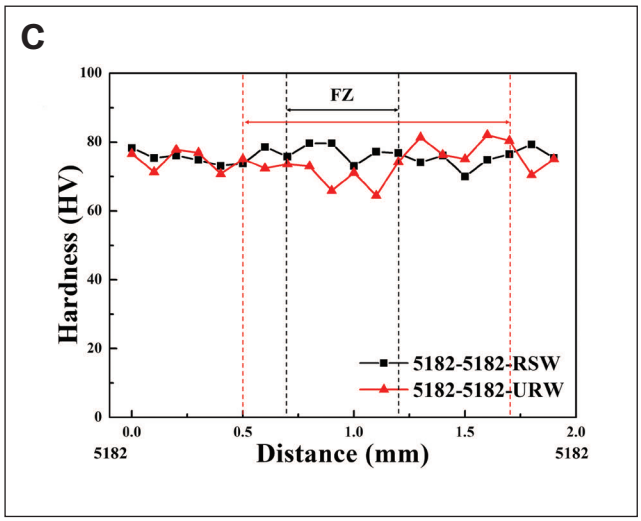

Fig. 13 — Hardness distribution of AA5182 in RSW (A) and URW (B) as well as hardness variation (C) along the white dashed arrow in A and B.

A more homogenized elemental distribution can also be anticipated from the enhanced flow. The hardness comparison in Fig. 12C indirectly shows that mixing is facilitated in URW. Since the RSW nugget was almost completely located on the AA7075 side, minimal mixing between the AA7075 and AA6111 was expected, and the nugget hardness basically followed the RSW of AA7075. In comparison, the position of the URW nugget was shifted toward the AA6111 side, which allowed dilutions of AA7075 with AA6111 composition. Since the hardness of AA6111 was lower than that of AA7075, the URW nugget's hardness with the mixed composition was lower than that of RSW regardless of its finer microstructure. A compositional analysis would be needed in future works to validate this element distribution assumption.

Both a lower thermal gradient and homogenized element distribution in the URW condition increased constitutional supercooling and facilitated equiaxed dendritic structure formation, as shown schematically in Fig. 15A. Furthermore, a higher number of heterogeneous nucleation sites was available from the collapse of cavitation bubbles as well as fragmented dendrites.

The narrower CCZ thickness in URW can be related to the balanced heat distribution and enlarged nugget. For the same welding time, the solidification rate increased as a result of larger nugget thickness. Along with the lower temperature gradient in URW, the higher solidification rate promoted the transition from planar to equiaxed dendritic growth, which reduced the CCZ's thickness in both the AA7075 and AA6111 sides. It was also consistent with the hardness map in Fig. 12B.

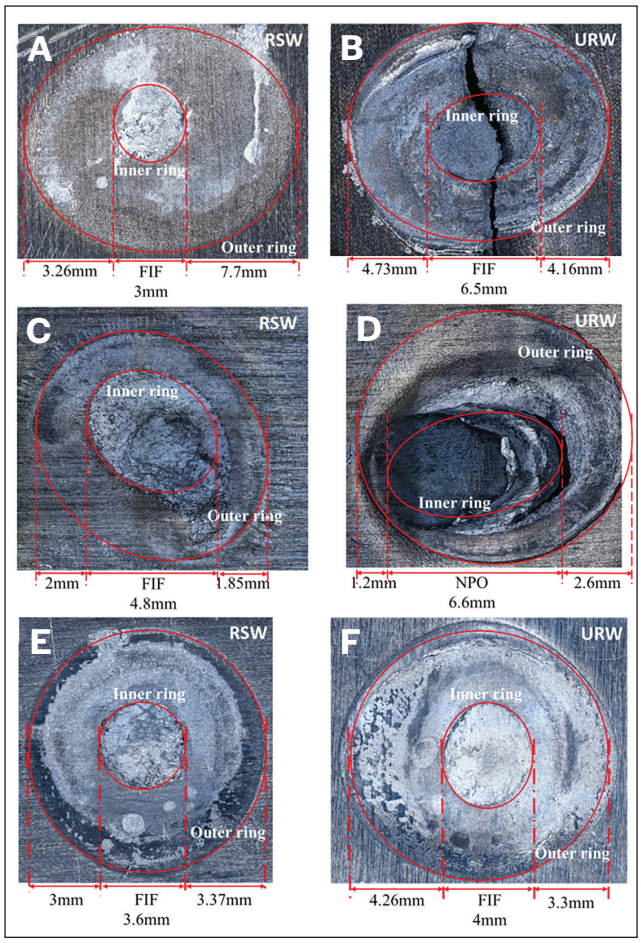

Fig. 14 — Fracture surfaces after the lap shear tensile tests: A, B — AA7075 side of AA7075–AA6111 RSW and URW welds; C, D — AA5182 RSW and URW welds; E, F — AA6111 RSW and URW welds. All samples were welded at 25 kA for 300 ms. (FIF: full interfacial failure; NPO: nugget pull out failure mode.)

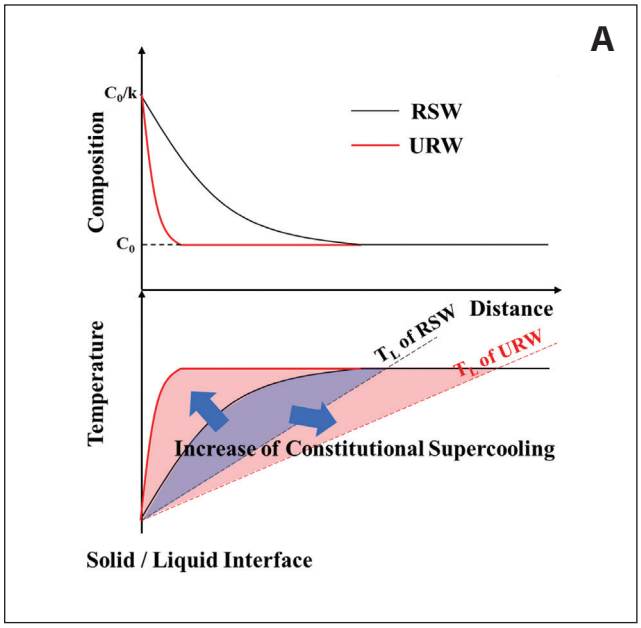

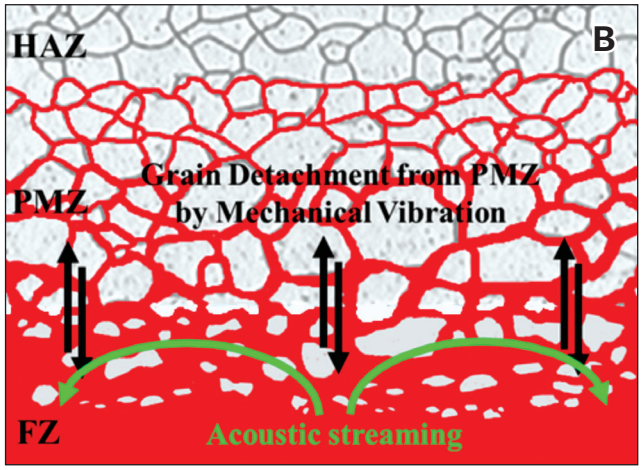

Fig. 15 — Schematic diagram of: A — Composition and temperature profile of RSW and URW at the solid-liquid interface, where constitutional supercooling was enhanced in URW; B — grain detachment from PMZ to FZ by UA.

The narrower PMZ in URW can be explained by the following: As the boundaries of the grains in the PMZ melted, these grains vibrated and detached from the solid substrate under ultrasonic mechanical agitation. The detached grains were then carried away into the molten nugget through acoustic streams, which enlarged the weld nugget and thinned the PMZ, as shown schematically in Fig. 15B. Shu et al. (Ref. 36) estimated a jet velocity of 100 m (32.8 ft)/s by acoustic cavitation, which can give a stress of 12.8 MPa at the dendritic root. Considering the yield strength of Al at the melting point was 6.5 MPa (Ref. 37), the liquid force from UA vibration should be sufficient to break the detached grains in the PMZ and reduce its width.

Similarly, in the AA7075–AA5182 stack, an unevenly positioned weld nugget was observed in RSW. In comparison, the URW nugget's position was more balanced. Furthermore, the nugget's geometry improved to a regular elliptical shape. The thicknesses of the CCZ and PMZ were also more reduced in URW than in RSW, and the mechanisms can be explained similarly to those of AA7075–AA6111. In the AA6111 stack, consistent microstructure improvements in URW welds were again achieved: The ECZ in the nugget center was promoted, and CCZ thickness was reduced.

Even though a unique ripened rosette microstructure was observed in the URW of AA5182 (Fig. 9B), the hardness of the weld nuggets was similar to that of the base metal, as shown in Fig. 13. These minimal hardness changes have also been reported in spot welds of AA5754 (Refs. 38, 39) and AA5052 (Ref. 19). Since 5xxx Al alloys are nonheat treatable, the effect of the thermal cycle during RSW was insignificant. This indicates that even though UA vibration produced a different microstructure in the nugget, its influence on hardness in the AA5182 welds was insignificant, as the overall change of hardness was small.

Failure Mode Analysis

The interfacial failure mode was partially caused by the insufficient nugget size, which was smaller than the critical value. The conventional AWS equation (Ref. 30) $4\sqrt{t}$ is only able to predict button pullout failure mode when sheet thickness is less than 1.5625 mm (0.16 in.). Sun et al. (Ref. 40) modified the equation with the addition of a porosity factor and calculated the critical nugget size based on the hardness of the nugget and the HAZ. The porosity factor f is defined as the ratio of the porosity-free area in the nugget to the total nugget area A_{total},

$$f = \frac{A_{total} - A_{porosity}}{A_{total}}, \quad 0 < f \leq 1.0 \tag{1}$$

where $A_{porosity}$ is the projected area of porosity in the fusion zone. Accordingly, the critical nugget size is:

$$D_{critical} = \frac{3.2t}{f} \tag{2}$$

where t is the sheet thickness. In welds with different thicknesses, the thinner one is used for calculations. For different weld stacks in this study, the critical nugget sizes based on AWS's and Sun's methods were calculated, and the results are presented in Table 4. Since almost no porosity was observed in all the welds in the studied condition as shown in the optical macrographs, the porosity factor f was assigned as 1.

In the AA7075–AA6111 weld, the individual sheet thickness was over 1.5625 mm (0.06 in.). Therefore, it was appropriate to use Sun's method. The average nugget sizes measured in both the RSW and URW welds were lower than the calculated

Table 4 — Comparison between Measured and Calculated Critical Nugget Size by Different Criteria

	Thickness (mm)	Measured Average Nugget Size (mm)		Critical Nugget Size (mm)	
				AWS (Ref. 30)	Sun (Ref. 40)
AA7075-AA6111	2.8/2.0	RSW	2.9	5.66	6.4
		URW	6.4		
AA7075-AA5182	2.8/1.5	RSW	3.1	4.90	4.8
		URW	4.1		
AA5182-AA5182	1.1/1.1	RSW	4.8	4.2	3.52
		URW	6.5		
AA6111-AA6111	2.0/2.0	RSW	3.5	5.66	6.4
		URW	4.0		

critical size, which showed the interfacial failure mode as experimentally observed. In the AA7075–AA5182 weld, the thickness of the AA5182 sheet was less than 1.5625 mm; therefore, the AWS method was adopted. The calculated critical nugget size was higher than the average measured value, which also agreed with the experimentally observed interfacial failure. In both dissimilar stacks, the relatively large thickness of the AA7075 sheet suppressed the tensile stress at the nugget circumference and base metal deformation, which restrained the nugget pullout. Furthermore, the nugget center was located unsymmetrically at the faying interface. The crack first initiated at the periphery of the weld and propagated along the CCZ since it had the lowest hardness in the weld and led to an interfacial fracture. As shown in Figs. 14A and B, the size of the inner ring in the RSW weld was much smaller than that of the ring in the URW weld. This can be attributed to the more-biased nugget position as well as the overall smaller nugget size in RSW.

In AA5182 welds, nugget pullout was observed in URW, whereas RSW showed the interfacial failure mode, as in Figs. 14C and D. Since the thickness of AA5182 was 1.1 mm in this stack, the critical nugget size calculation followed the AWS standard. As shown in Table 4, the measured average URW nugget size was significantly larger than the critical value, which agreed with the pullout mode. The thinness of the AA5182 sheet enabled an increased rotation of the nugget during lap shear tensile tests. As the rotation angle increased, the shear stress at the weld centerline reduced. In RSW, the measured average nugget size was slightly larger than the calculated critical size. On the other hand, because of the variation in actual experimental nugget size, the interfacial failure mode was still observed.

Both AA6111 RSW and URW exhibited interfacial failure, as in Figs. 14E and F. The inner ring was larger in URW, which matched the microstructure of a larger nugget size. The AA6111 thickness was larger than 1.5625 mm, and Sun's method was employed. The measured average nugget sizes in RSW and URW were smaller than the critical value, which agreed with the interfacial failure. Additionally, the outer ring was wider and possessed a more bonded area in URW. Ultrasonic vertical vibration of the bottom sheet before actual melting facilitated the breakdown of the surface oxide layer and formation of the nascent interface, which allowed the welding current to pass through more locations and promoted bonding at the outer ring.

Strength Enhancement Mechanism of URW

As shown in Fig. 2, the ultrasonic benefits on lap shear tension properties were generally more significant at longer welding times. This was because a longer welding time enabled more interaction between the ultrasonic field and molten metal, which led to a more effective enhancement of the process. Ultrasonic effects also varied depending on the specific alloy's composition.

Figure 16 summarizes the average and standard deviation of nugget size and lap shear tensile strength of RSW and URW at different welding conditions. The nugget size was measured based on the inner ring on the fracture surface after lap shear tensile tests. Among different pairs of Al alloys, the URW welds consistently exhibited a larger nugget size and higher maximum lap shear tensile load. For spot welds, mechanical strength relied on both the nugget size and microstructure. To reveal the factor that dominated strength enhancement, linear fitting between nugget size and lap shear tensile strength in all the welding conditions was performed, and the results are provided in Fig. 17.

In AA5182–AA7075 and AA6111–AA6111, the relationship between nugget size and weld strength in URW was above that in RSW. In AA7075–AA6111, URW also showed higher strength than the linear extrapolation of RSW. In other words, for these three pairs of materials, with the same nugget size,

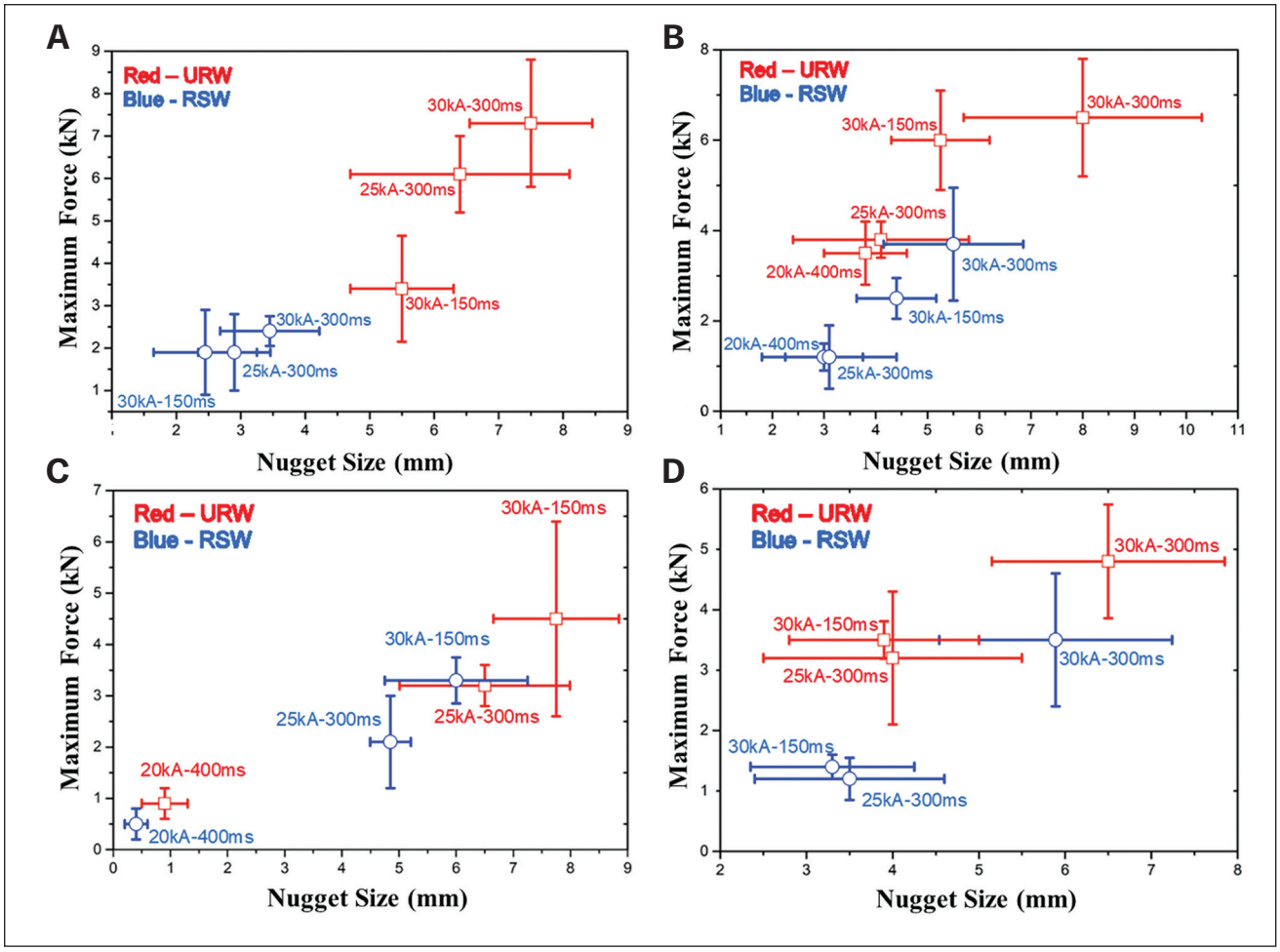

Fig. 16 — Relationship between maximum lap shear tensile load and nugget size of RSW and URW welds at different conditions: A — AA7075 to AA6111; B — AA7075 to AA5182; C — AA5182; D — AA6111.

URW possessed a higher strength than RSW, indicating that microstructure modification was a contributing factor. As shown in Figs. 5 and 6, both the narrower CCZ and the more symmetric nugget position contributed to strength enhancement in the two dissimilar Al stacks. For the AA6111 weld, the ECZ was achieved in URW, whereas the RSW nugget only contained a columnar structure.

In AA5182 welds, the relationship between strength and nugget size followed a roughly similar trend between URW and RSW. In other words, if the same nugget size was reached, the strengths of the RSW and URW welds were similar. This indicated URW strength enhancement mainly came from the enlarged nugget. As shown in the microhardness results in Fig. 13, the hardness difference was minimal between the weld nugget and base material in both URW and RSW of AA5182 welds. Accordingly, nugget size was a more dominant factor.

Conclusion

This study included a comprehensive experimental analysis of URW of various pairs of similar and dissimilar Al alloys. The main conclusions are:

1) URW consistently showed enhanced mechanical behavior in lap shear tensile and cross-tension tests for various stacks of Al alloys under different welding conditions. The ultrasonic benefits were more effective at a longer welding time.

2) Weld microstructure was improved by UA in multiple aspects of larger nugget size, promoting the formation of the ECZ at the center, and a narrower CCZ and PMZ at the nugget periphery. Specifically, for dissimilar Al welds, UA vibration can move the unsymmetric nugget in a more-balanced way toward the weld interface.

3) For dissimilar Al welds, the narrower CCZ and balanced nugget position were contributing to URW strength improvement in addition to the enlarged nugget size. In the nonheat-treatable AA5182 welds, since nugget hardness was approximately the same in RSW and URW welds, nugget size was a more dominant strength factor.

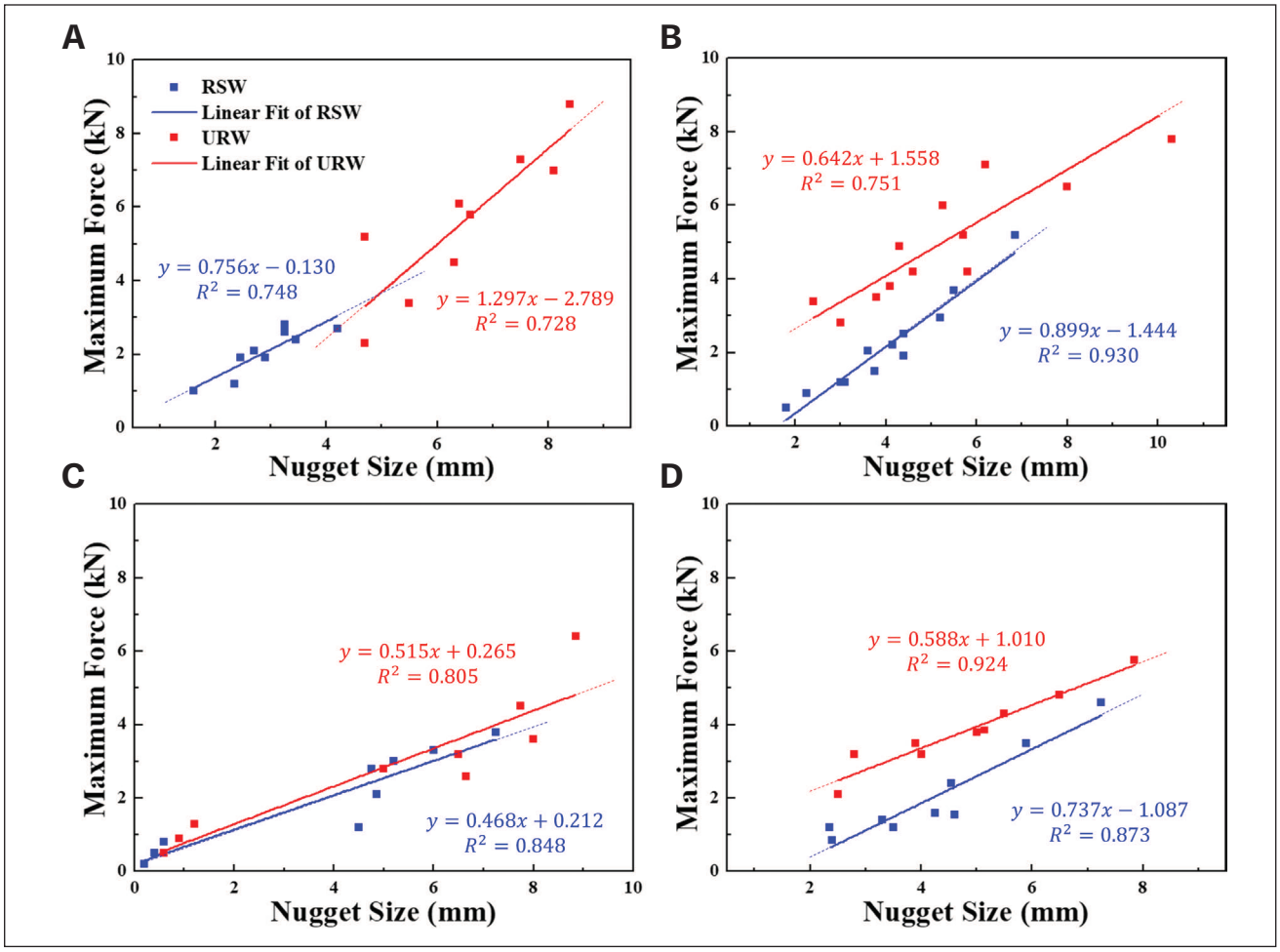

Fig. 17 — Linearly fitted relationship between maximum lap shear tensile load and nugget size of RSW and URW welds at different conditions: A — AA7075 to AA6111; B — AA7075 to AA5182; C — AA5182; D — AA6111.

A compositional analysis will be performed in future works to understand microstructure improvement through homogenizing elemental distribution.

Acknowledgments

The project was supported by the National Science Foundation under grant #1853632: An innovative hybrid ultrasonic resistance welding process for joining advanced lightweight and dissimilar materials. Aluminum materials were provided by Novelis. The authors would also like to acknowledge the help of Wayne Papageorge in preparing the metallurgical samples.

References

1. Arroyo, F. R. A. M., and Miguel, L. J. 2019. The trends of the energy intensity and CO_2 emissions related to final energy consumption in Ecuador: Scenarios of national and worldwide strategies. *Sustainability* 12: 1–21. DOI: 10.3390/su12010020

2. Wang, C. 2013. Changing energy intensity of economies in the world and its decomposition. *Energy Economics* 40: 637–644. DOI: 10.1016/j.eneco.2013.08.014

3. Yılmaz, T., Tüfekçi, M., and Karpat, F. A. 2017. Study of lightweight door hinges of commercial vehicles using aluminum instead of steel for sustainable transportation. *Sustainability* 9: 1661. DOI: 10.3390/su9101661

4. Hao, M., Osman, K. A., Boomer, D. R., and Newton, C. J. 1996. Developments in characterization of resistance spot welding of aluminum. *Welding Journal* 75(1): 1-s to 14-s.

5. Shah, U., and Liu, X. 2020. Effect of ultrasonic energy on the spot weldability of aluminum alloy AA6061. *Materials and Design* 192: 108690. DOI: 10.1016/j.matdes.2020.108690

6. Ni, Z. L., and Ye, F. X. 2018. Ultrasonic spot welding of aluminum alloys: A review. *Journal of Manufacturing Processes* 35: 580–594. DOI: 10.1016/j.jmapro.2018.09.009

7. Lee, S. S., Kim, T. H., Hu, S. J., Cai, W. W., and Abell, J. A. 2011. Joining technologies for automotive lithium-ion battery manufacturing: A review. *ASME 2010 International Manufacturing Science and Engineering Conference* 1: 541–549. New York, N.Y.: ASME. DOI: 10.1115/MSEC2010-34168

8. Matheny, M. P., and Graff, K. F. 2015. "Ultrasonic welding of metals." In *Power Ultrasonics*, edited by Gallego-Juárez, J. A., and Graff, K. F., 259–293. Sawston, Cambridge: Woodhead Publishing. DOI: 10.1016/B978-1-78242-028-6.00011-9

9. Bakavos, D., and Prangnell, P. B. 2010. Mechanisms of joint and microstructure formation in high power ultrasonic spot welding 6111 aluminium automotive sheet. *Materials Science and Engineering: A* 527: 6320–6334. DOI: 10.1016/j.msea.2010.06.038

10. Manladan, S. M., Yusof, F., Ramesh, S., Fadzil, M., Luo, Z., and Ao, S. 2017. A review on resistance spot welding of aluminum alloys.

The International Journal of Advanced Manufacturing Technology 90: 605–634. DOI: 10.1007/s00170-016-9225-9

11. Fukumoto, S., Lum, I., Biro, E., Boomer, D. R., and Zhou, Y. 2003. Effects of electrode degradation on electrode life in resistance spot welding of aluminum alloy 5182. *Welding Journal* 82(11): 307-s to 312-s.

12. Crinon, E., and Evans, J. T. 1998. The effect of surface roughness, oxide film thickness and interfacial sliding on the electrical contact resistance of aluminium. *Materials Science and Engineering A* 242: 121–128. DOI: 10.1016/S0921-5093(97)00508-X

13. Chang, B. H., Du, D., Sui, B., Zhou, Y., Wang, Z., and Heidarzadeh, F. 2006. Effect of forging force on fatigue behavior of spot welded joints of aluminum alloy 5182. *Journal of Manufacturing Science and Engineering* 129: 95–100. DOI: 10.1115/1.2383071

14. Al Naimi, I. K., Al Saadi, M. H., Daws, K. M., and Bay, N. 2015. Influence of surface pretreatment in resistance spot welding of aluminum AA1050. *Production & Manufacturing Research* 3: 185–200. DOI: 10.1080/21693277.2015.1030795

15. Luo, Z., Ao, S., Chao, Y. J., Cui, X., Li, Y., and Lin, Y. 2015. Application of pre-heating to improve the consistency and quality in AA5052 resistance spot welding. *Journal of Material Engineering and Performance* 24: 3881–3891. DOI: 10.1007/s11665-015-1704-x

16. Deng, L., Li, Y. B., Carlson, B. E., and Sigler, D. R. 2018. Effects of electrode surface topography on aluminum resistance spot welding. *Welding Journal* 97(4): 120-s to 132-s. DOI: 10.29391/2018.97.011

17. Wang, Y., Tao, W., and Yang, S. 2019. A method for improving joint strength of resistance spot welds of AA 5182-O Aluminum Alloy. *Journal of Manufacturing Processes* 45: 661–669. DOI: 10.1016/j.jmapro.2019.07.024

18. Li, M., Wang, Y., Yang, S., Tao, W., and Zhang, G. 2021. Improving mechanical properties and electrode life for joining aluminum alloys with innovatively designated Newton ring electrode. *Journal of Manufacturing Processes* 64: 948–959.DOI: 10.1016/j.jmapro.2021.02.001

19. Li, Y., Luo, Z., Yan, F., Duan, R., and Yao, Q. 2014. Effect of external magnetic field on resistance spot welds of aluminum alloy. *Materials & Design (1980-2015)* 56: 1025–1033. DOI: 10.1016/j.matdes.2013.12.005

20. Huang, M., Zhang, Q., Qi, L., Deng, L., and Li, Y. 2020. Effect of external magnetic field on resistance spot welding of aluminum alloy AA6061-T6. *Journal of Manufacturing Processes* 50: 456–466. DOI: 10.1016/j.jmapro.2020.01.005

21. Qi, L., Zhang, Q., Ma, Y., Xu, Y., Han, X., and Li, Y. 2021. A comparative study on mechanical performance of traditional and magnetically assisted resistance spot welds of A7N01 aluminum alloy. *Journal of Manufacturing Processes* 66: 133–144. DOI: 10.1016/j.jmapro.2021.04.006

22. Shah, U. H., and Liu, X. 2019. Ultrasonic resistance welding of TRIP-780 steel. *Journal of Materials Processing Technology* 274: 116287. DOI: 10.1016/j.jmatprotec.2019.116287

23. Novelis Advanz™ 7UHS – s701, Novelis. Retrieved on July 28, 2022, from *novelis.com/product/novelis-advanz-7uhs-s701/*.

24. Novelis Advanz™ 6HS – s650, Novelis. Retrieved on July 19, 2022, from *novelis.com/product/novelis-advanz-6hs-s650/*.

25. Metal, Plastic, and Ceramic Search Index. Retrieved on July 19, 2022, from *matweb.com/Search/MaterialGroupSearch.aspx?GroupID=201*.

26. Marashi, S. P. H., Pouranvari, M., Salehi, M., Abedi, A., and Kaviani, S. 2010. Overload failure behaviour of dissimilar thickness resistance spot welds during tensile shear test. *Materials Science and Technology* 26: 1220–1225. DOI: 10.1179/026708309X12506933872702

27. Eskin, D. G. 2017. Ultrasonic processing of molten and solidifying aluminium alloys: overview and outlook. *Materials Science and Technology* 33: 636–645. DOI: 10.1080/02670836.2016.1162415

28. Flemings, M. C. 1991. Behavior of metal alloys in the semisolid state. *Metallurgical Transactions A* 22: 957–981.

29. Li, Y., Zhang, Y., Luo, Z., Shan, H., Feng, Y. Q., and Ling, X. Z. 2016. Failure mode transition of triple-thin-sheet aluminum alloy resistance spot welds under tensile-shear loads. *Welding Journal* 95(12): 479-s to 490-s.

30. Sawhill, J. M., Watanabe, H., and Mitchell, J. W. 1977. Spot weldability of Mn-Mo-Nb, V-N and SAE 1008 steels. *Welding Journal* 56(7): 217-s to 224-s.

31. Pouranvari, M., Asgari, H. R., Mosavizadch, S. M., Marashi, P. H., and Goodarzi, M. Effect of weld nugget size on overload failure mode of resistance spot welds. *Science and Technology of Welding and Joining* 12: 217–225. DOI: 10.1179/174329307X164409

32. Hayat, F. 2012. Effect of aging treatment on the microstructure and mechanical properties of the similar and dissimilar 6061-T6/7075-T651 RSW joints. *Materials Science and Engineering: A* 556: 834–843. DOI: 10.1016/j.msea.2012.07.077

33. Shah, U., Liu, X., Benatar, A., Kuprienko, A., and Zhang, W. Computational analysis of the ultrasonic effects on resistance spot welding process. *Journal of Manufacturing Processes* 81: 191–201. DOI: 10.1016/j.jmapro.2022.06.050

34. David, S. A., and Vitek, J. M. 1989. Correlation between solidification parameters and weld microstructures. *International Materials Reviews* 34: 213–245. DOI: 10.1179/imr.1989.34.1.213

35. Kou, S. 2003. *Welding Metallurgy* 2nd Ed., 431: 223–225. New Jersey: John Wiley & Sons.

36. Shu, D., Sun, B., Mi, J., and Grant, P. S. 2012. A high-speed imaging and modeling study of dendrite fragmentation caused by ultrasonic cavitation. *Metallurgical and Materials Transactions A* 43: 3755–3766. DOI: 10.1007/s11661-012-1188-3

37. Pilling, J., and Hellawell, A. 1996. Mechanical deformation of dendrites by fluid flow. *Metallurgical and Materials Transactions A* 27: 229–232. DOI: 10.1007/BF02647763

38. Senkara, J., and Zhang, H. 2000. Cracking in spot welding aluminum alloy AA5754. *Welding Journal* 79(7): 194-s to 201-s.

39. Shi, Y., and Guo, H. 2013. Fatigue performance and fatigue damage parameter estimation of spot welded joints of aluminium alloys 6111-T4 and 5754. *Fatigue & Fracture of Engineering Materials & Structures* 36: 1081–1090. DOI: 10.1111/ffe.12089

40. Sun, X., Stephens, E. V., Davies, R. W., Khaleel, M., and Spinella, D. J. 2004. Effects of fusion zone size on failure modes and static strength of aluminum resistance spot welds. *Welding Journal* 83(11): 308-s to 318-s.

HO KWON, **UMAIR SHAH**, and **XUN LIU** (*liu.7054@osu.edu*) are with the Department of Materials Science & Engineering, The Ohio State University, Columbus, Ohio. **JULIO MALPICA**, **PATRICK LESTER**, and **HARINI BONAM** are with Novelis Corp., Atlanta, Ga.

Rapid Publication of Cutting-Edge Welding Research — *WJRS Letters*

Dear Researchers,

The *Welding Journal Research Supplement* (*WJRS*) is seeking manuscripts for rapid publication of **emerging research that is cutting edge and novel**. The manuscripts are relatively short in length and will be called *WJRS Letters. They are aimed at allowing authors to quickly publish new research results on "hot" topic areas of interest to the WJRS.*

Editor approval is required for submission of *WJRS Letters* manuscripts. If you are interested, please submit an abstract summarizing your proposed manuscript. *WJRS Letters* are not intended to be data dumps or options for publications of low-quality research. Abstracts that do not describe new, cutting-edge research will be declined. If your abstract is accepted, you'll be invited to submit a manuscript. Below are more details.

(1) First, provide an abstract < 500 words, which includes author names, emails, and affiliations, to *wjrs@aws.org*.

A *single figure* (not multipart) with a caption can also be provided with the abstract. **Complete manuscripts submitted without approval will be declined immediately. Do not submit abstracts or manuscripts to the *WJRS* submission website.**

(2) If your abstract is accepted, you'll be invited to write a manuscript of not more than 2200 words with three to four figures (with captions). You will receive a template for your *Letters* after abstract approval; visit *aws.org/library/doclib/WJRS-guidelines.pdf*. All content must fit into **five** pages when laid out in the current *WJRS* format reflected in the template. Manuscript content must fit into the template without format changes to be published.

(3) Manuscripts will require succinct, focused communication with the following sections:

- **Introduction/Background/Objectives**
- **Procedures**
- **Results**
- **Discussion**
- **Conclusions**
- **Limited References**

If you have questions, please email *wjrs@aws.org*. Thank you for supporting this effort.

Sincerely,

Thomas J. Lienert, PhD, FASM, FAWS
Review Editor

AWS American Welding Society